Korean J. Chem. Eng., **31**(8), 1413-1424 (2014)
DOI: 10.1007/s11814-014-0075-6

pISSN: 0256-1115
eISSN: 1975-7220

Deposition of toxic metal particles on rough nanofiltration membranes

Oluranti Agboola*,†, Jannie Maree, Richard Mbaya*, Caliphs Musa Zvinowanda**, Gomotsegang Fred Molelekwa***, Nora Jullok***, Bart Van der Bruggen***, Alexander Volodine****, and Chris Van Haesendonck****

*Department of Chemical Engineering, Tshwane University of Technology, Pretoria, South Africa
**Department of Environmental Water and Earth Science, Tshwane University of Technology, Pretoria, South Africa
***Process Engineering for Sustainable Systems, Department of Chemical Engineering, KU Leuven, W. de Croylaan 46, B-3001 Heverlee, Belgium
****Solid State Physics and Magnetism Section, KU Leuven, Celestijnenlaan 200d, Box 2414, B-3001 Heverlee, Belgium
(*Received 24 January 2014 • accepted 27 February 2014*)

Abstract–Two nanofiltration (NF90 and Nano-Pro-3012) membranes were investigated for their capacity to remove metal ions. This study presents the effect of membrane roughness on the removal of toxic metal ions during dead end membrane filtration. Atomic force microscopy, scanning electron microscopy, WSXM software and ImageJ were used to characterize the roughness of the membranes. Gradual decrease in filtration permeate flux was observed as foulants accumulated at the interface of the membranes; filtration permeate flux varied from 20 L/m^2/h to 14 L/m^2/h and 11 L/m^2/h to 6 L/m^2/h for NF90 and Nano-Pro-3012, respectively. NF90 membrane was more prone to fouling than the Nano-Pro-3012 membrane: the percentage flux reduction was higher for NF90 (3.6%) than Nano-Pro-3012 (0.98%). The bearing ratio of the fouled NF90 exhibited a high peak of 7.09 nm than the fouled Nano-Pro-3012 with the peak of 6.8 nm.

Keywords: Particle Deposition, Flux Reduction, AFM, SEM, Roughness, Bearing Analysis

INTRODUCTION

Membrane technology has played an important role towards improving the performance of a large number of industrial processes [1]. Membrane separation processes have been used in many industries because of their selectivity and adaptability characteristics. The rate at which solutes and solvents are transferred across a membrane is controlled by a driving force, and the rate at which solutes are been rejected depends on the size and shape of the solute molecules. Nanofiltration membranes have separation characteristics between those of ultrafiltration and reverse osmosis membranes [2,3]. Nanofiltration is often used in desalination processes and for water with low total dissolved solids for water softening, i.e., removal of cations. Nanofiltration is sometime used together with reverse osmosis in order for permeate to reach the standard of drinking water quality.

During the filtration of aqueous solutions of charged compounds such as salts or organic acids, the membrane surface charge is largely affected by its interaction with the feed components [4]. In practice, the deposition of solutes or dispersed materials on the membrane surface makes membrane fouling inevitable. The characteristics capable of influencing fouling are membrane chemical characteristics such as material composition, surface charge, hydrophobicity and structural characteristics such as porosity, roughness, pore size, pore shape and pore size distribution together with the dissolved constituent in water such as organic, mineral or biological pollutants, suspended and/or dissolved matter. However, fouling during filtration of colloidal solutions is attributed to surface roughness of the membranes [5-8]. Particles are thought to accumulate preferentially in the "valleys" of rough membranes, resulting in "valley clogging." Therefore, a rough membrane generally shows more fouling than a smooth membrane [4]. Most of the characteristics of commercial nanofiltration membranes are unknown because of patented production processes by manufacturers [9,10]. Most thin-film composite nanofiltration membranes are prepared by a polymerization process in the border area between two very reactive bi-functional or tri-functional monomers that react with each other in the water or in an organic solvent, resulting in a significant network structure [10-12]. The adaptability, stability and efficiency of thin-film composite membranes depend on their dense layered structure, consisting of different polymeric materials such as cellulose, polysulphone, polyamide, silicone, and may vary under some filtration conditions [12].

Advances in the study of membrane structure have been made possible through techniques like transmission electron microscopy [10, 13,14], scanning electron microscopy [15,16], atomic force microscopy [14,17-21] which have helped researchers to understand the structural characterization of membranes. Measurements at the nanoscale which will incorporate the effects of surface morphology can therefore be done using these measurement techniques. The characterization of membrane by atomic force microscopy is one of the numerous methods in membrane characterization. Atomic force microscopy is a probe scanning technique commonly used to image surfaces for producing three-dimensional images; however, an important advantage of atomic force microscopy in the study of surface properties of materials, including membrane, is the ability to quan-

†To whom correspondence should be addressed.
E-mail: sadikuo@tut.ac.za, funmi2406@gmail.com

tify both surface morphology and surface interactions with a single instrument [18]. Atomic force microscopy can be used under three modes: contact, non-contact and tapping [22]. This technique provides a high-resolution representation of the surface (1 nm) and gives information such as roughness, pore size, pore density and/or pore size distribution [23]. Surface roughness is an important structural property of nanofiltration membranes [24] that can be attributed to colloidal fouling [7,25-28]. The continuous reduction in permeate flux due to the increase in hydrodynamic resistance of the growing cake layer is referred to as colloidal membrane fouling. Understanding the loss of the efficiency of membranes presents a challenge, since it requires methods capable of providing an insight into the characteristics of the selective layer and the changes in these characteristics upon loss of efficiency. We used two nanofiltration membranes as a model system to study the structural and morphological changes that take place in the membrane upon exposure to mixed salt solution and to correlate this data to membrane process performance.

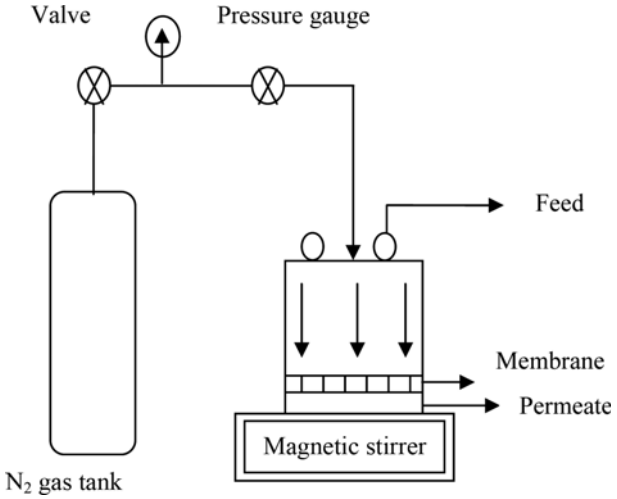

Fig. 1. Schematic diagram showing a dead end cell.

MATERIALS AND METHODS

1. Nanofiltration Membranes Characteristics

Two nanofiltration membranes (Nano-Pro-3012 and NF90) were chosen for this research, as a representative of a class of membranes which are acid stable in water treatment applications. The salts used in preparing the synthetic solutions are analytical salts and the approximate compositions of the salts used in preparing the synthetic solution are listed in the Table 1. The approximate compositions of the salts used in preparing the synthetic solutions are based on the approximate compositions of heavy metals found in the AMD from shaft 8 at Rand Uranium wastewater treatment plant in Randfontein, South Africa. The pH of the solution was controlled with NaOH. The operating conditions of the NF membranes are shown in Table 2. The solute of the mixed salt was analyzed by inductively coupled plasma optical emission spectrometer. The solution pH and temperature were measured with a pH meter (Mettler Toledo FG20) and thermometer, respectively.

2. Filtration Experiments

The membrane sheet was initially rinsed with distilled water and was used to measure the clean water flux using distilled water before the mixed metal solution was used with the system for each tested condition. The clean water flux experiments were done at stirring velocity rate of 500 rpm to ascertain whether the membrane did foul. After filtration was terminated, the membrane was cleaned with deionized water, followed by a clean water flux measurement.

3. Flux Decline Experiments with Laboratory Dead End Cell

The investigation was done using a 1,000-ml dead-end membrane filtration apparatus with magnetic stirrer as shown in Fig. 1. The membrane tested was placed in the cell. The experiments were carried out with one liter of solution containing the metal ions at different concentrations. The concentrations of the metals are shown in Table 1. The membrane active area is about 0.01075 m^2. A membrane sheet was fitted to the cell. The solution of the mixed salts was placed in the cell at the product inlet. An operating pressure of 10 bar was employed via high-pressure regulator and a nitrogen gas cylinder. The permeate flux was collected in a beaker on the electrical balance and permeate mass was determined.

4. Analysis of Results

The pure water flux was determined by weighing the obtained permeate during a predetermined time using an electronic balance. Osmotic pressure is a colligative property directly proportional to concentration. For membrane permeability measured by distilled water runs, the osmotic pressure in this case is zero. Assuming constant (pure water permeability), L_p, the volume flow across the membrane can be given as [29]:

$$J_v = L_p * \Delta P \quad (1)$$

By plotting permeate flux (J_v) for a variation of applied pressure (ΔP), the membrane permeability, L_p for distilled water and solution concentration can be obtained from the slope of the straight line as follows [29]:

Table 1. Composition of salts used in the experiment

Metals	Composition mg/L
Co^{2+}	5
Fe^{2+}	600
Mg^{2+}	100
Ni^{2+}	10
Mn^{2+}	150

Table 2. Nanofiltration membrane operating properties

NF membrane	Maximum operating pressure	Minimum operating pressure	Maximum operating temp.	Allowable pH	Minimum recirculation flowrate	Maximum recirculation flowrate
Nano-Pro-3012	40 Bar (580 psi)	10 Bar (145 psi)	50 °C (122 °F)	0-12	90 L/min (24 gpm)	280 L/min (74 gpm)
NF90	20 Bar (290 psi)	4.8 Bar (70 psi)	45 °C (113 °F)	2-11	1.4 m^3/hr (6 gpm)	3.6 m^3/hr (16 gpm)

$$L_p = \frac{J_v}{\Delta P} \tag{2}$$

The permeate flux and rejection were investigated as a function of working parameters such as operating time and water recovery. The permeate flux J_v L/m^2/h was determined by measuring the volume of permeate collected in a given time interval divided with membrane area by the relation in Eq. (3) [29].

$$J_v = \frac{Q}{A} \tag{3a}$$

where, Q and A represent flow rate of permeate and the membrane area, respectively. The flux reduction with regards to clean water flux can be determined as a percentage of flux by comparing the flux before and the flux after membrane operation using Eq. (3b) [29]:

$$FR_{CWF} = \frac{J_{vb} - J_{va}}{J_{vb}} \times 100 \tag{3b}$$

Here, the indices a and b are ascribed to before and after filtration of feed. The observed rejection, which is the measure of how well a membrane retains a solute, was calculated by the relation in Eq. (4) [29].

$$\%R = \left(1 - \frac{C_p}{C_i}\right) \times 100 \tag{4}$$

where C_p and C_i are the solution concentrations in the permeate and in the initial feed solution, respectively.

5. Analysis of Surface Roughness Using Atomic Force Microscopy (AFM)

Clean membranes were cut into small pieces and glued onto a sample holder with an agar tape before non-contact atomic force microscopy imaging was performed using an Agilent Technologies 5500 scanning probe microscope (PicoPlus-Atomic Force Microscopy Series 5500). The AFM cantilever used was made of silicon (Nanosensors) with a resonant frequency of ~60 kHz, a nominal spring constant of 7.4 N/m with a typical tip radius of less than 7 nm. The atomic force microscopy measurements were performed on dry membranes in an air atmosphere with relative humidity of ~30%. The AFM images were flattened with order 1 and the *rms* (root-mean-squared) value of the roughness was obtained by using the Nanotechnology Research Tool [30]. The roughness depends on the scan size; thereby for the comparative analysis it is required that roughness is obtained from images with the same scan areas [23]. The atomic force microscopy images of NF90 and Nano-Pro-3012 membranes used in the roughness analysis test were done for two different scan areas. The membrane surface roughness was determined with the atomic force microscopy and was further analyzed with WXSM 5.0 software for bearing ratio analysis.

Several statistical parameters that were used to quantitatively describe the surface roughness of the membranes are summarized in Table 3. Some of the parameters are compared with the parameters obtained from ImageJ software. The parameters were recorded for 1.0 μm×1.0 μm and 5.0 μm×5.0 μm scan areas for the clean membranes and 5.0 μm×5.0 μm scan area for the fouled membranes.

6. AFM Characterization

The growth of scanning probe microscopy has been parallel to the revolution of computer technologies. In fact, computers have played a central role in the development of this technique significantly by improving the data acquisition, control, image processing, and data analysis [30]. WSXM 5.0 software was introduced as a program that can be widely used by the scanning probe microscopy community. Membrane roughness parameters were extracted from non-contact mode atomic force microscopy topography image using instrument's software (WXSM 5.0 software) in conjunction with scanning probe microscopy [30]. Phase imaging is an extension of non-contact mode atomic force microscopy. It was used to enhance the contrast for the features of interest, providing additional information to the topographical projections [31].

7. Scanning Probe Microscopy Image Process - Roughness Analysis

Surfaces of the nanofiltration membranes were compared in terms of roughness parameters, such as root mean square *rms* (nm), the mean roughness *ra* (nm), surface skewness (S), and surface kurtosis (K). The roughness parameters depend on the curvature and the size of the atomic force microscopy tip and the treatment of the captured surface data (plane fitting, flattering, filtering, etc.). The root mean square (*rms*) roughness parameter is a statistical measure of the relative roughness of a surface and is essentially the standard deviation of the heights for all the pixels in the image from the arithmetic mean. The root mean square of the roughness varies with the interval range; it is given by the following expression [30]:

$$rms = \sqrt{\frac{\sum_{ij} (a_{ij} - \langle a \rangle)^2}{N}} \tag{5}$$

where a_{ij} is the height value for a particular point on the image (nm), $\langle a \rangle$ is the average/mean height of all the pixels in the image (nm) and N is the total number of pixels within the image. The maximum range is the height difference between the lowest and highest pixels in the image. The mean roughness is the mean value of the surface relative to the center plane, the plane for which the volumes enclosed by the image above and below this plane are equal, it shows how much rough the sample is:

$$r.a = \frac{\sum_{ij} |a_{ij} - \langle a \rangle|}{N} \tag{6}$$

The average height ($\langle a \rangle$) is the mean height of the pixel in the image. It is given by the following expression:

$$\langle a \rangle = \frac{\sum_{ij} a_{ij}}{N} \tag{7}$$

The surface skewness (S) is the measure of the direction of the asymmetry of the distribution of heights in the sample:

$$S = \frac{\sum_{ij} (a_{ij} - \langle a \rangle)^3}{N\sigma^3} \tag{8}$$

where:

$$\sigma = \sqrt{\frac{\sum_{ij} (a_{ij} - \langle a \rangle)^2}{N}} \tag{9}$$

The surface kurtosis (K) is the measure of the degree of peakedness in the distribution of heights in the membranes comparing it to the normal distribution. This statistical parameter is given by the

expression in Eq. (10).

$$K = \frac{\sum_{ij}(a_{ij} - \langle a \rangle)^4}{N\sigma^4} \quad (10)$$

where:

$$\sigma = \sqrt{\frac{\sum_{ij}(a_{ij} - \langle a \rangle)^2}{N}} \quad (11)$$

8. Bearing Analysis

The bearing analysis was used to work out the height information regarding this study and the methodology used will be described briefly. The term "bearing" refers to the relative roughness of the sample surface regarding the high and low area. In bearing analysis, the depths of all pixels of the image with a particular reference point, e.g., the highest pixel, are analyzed. This type of analysis gives the estimation of the surface covered and the estimation of depths possible, for either the entire image or for a selected area. Bearing analyses plot the height distribution over the membrane sample. It is a measure of how much of the surface lies above and below a certain height; it gives an indication of height distribution over the surface. The bearing ratio gives the percentage of the surface that lies above and below the arbitrary chosen height. For clean membranes, bearing analysis was used to determine the roughness with regards to the height distribution. For fouled membranes, bearing analysis gives quantitative information about what fraction of the deposited metals are located above or below a specific bearing plane.

9. Scanning Electron Microscopy (SEM)

The setup used to visualize the surfaces of the membranes was a Joel Field Emission Electron Microscope JESM-7600F. The virgin and used membranes were mounted on a double-sided carbon tape and the surfaces were coated with iridium (5 nm thickness) to make it conductive before SEM studies. The sample was exposed to an electron beam at an accelerating voltage of 15 kV to get a signal for the SEM studies. The micro-marker on the micrographs was used to estimate the pore size (diameter). The SEM images were analyzed using NIH ImageJ software.

10. NIH ImageJ Software

ImageJ is a public domain Java image processing and analysis program inspired by NIH image for Macintosh. It can calculate area and pixel value statistics of user-defined selections. It can measure distances and angles, and can create density histograms and line profile plots. It supports standard image processing functions such as contrast manipulation, sharpening, smoothing, edge detection and median filtering. ImageJ allows the systematic extraction of key parameters values such as total area, average size, % area, mean grey value, maximum and minimum grey value, standard deviation, angle, centroid, circularity, surface skewness and surface kurtosis. For the purpose of this work, average height, kurtosis, and skewness were studied. The mean grey value can be defined as the average grey value within the selected region of a sample. The ImageJ reported values will be compare with the WXSM 5.0 software reported values.

RESULTS AND DISCUSSION

1. Membrane Permeability

Pure water flux measurement as a function of trans-membrane pressure was carried out for the nanofiltration membranes to investigate the porosity of the membranes. The experiments were run for 120 min. It was observed that increase in the pressure across the membrane also increases the flux for both membranes and the permeate fluxes changed linearly with the trans-membrane pressure. The flux of NF90 was much higher than Nano-Pro-3012 because NF90 was more porous. Using Eq. (2), the membrane permeability (L_p) of Nano-Pro-3012 and NF90 was found to be 1.37 L/m^2/h/bar and 5.7 L/m^2/h/bar, respectively (Fig. 2); this could be due to difference in pore sizes of the membranes, thus the need to investigate their pore sizes. It was decided to continue the experiments for NF90 and Nano-Pro-3012 at 10 bar for comparison of results.

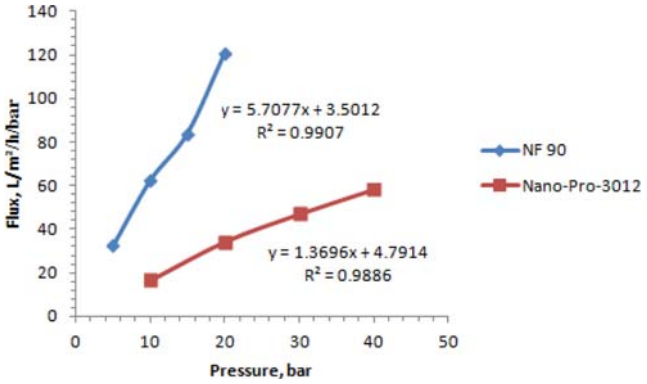

Fig. 2. Water Flux of deionized water as function transmembrane pressure.

2. The Morphology of the Membranes

It is possible to observe the membrane skin layers (top views) with scanning electron microscopy (Fig. 3). Membrane surface features with respect to the pore size were investigated using scanning electron microscopy by analyzing the pore diameter and the interpore spacing. The scanning electron microscopy image analysis was done using ImageJ software. Fig. 3 shows the original scanning electron microscopy images of Nano-Pro-3012 and NF90; and the threshhold images of Nano-Pro-3012 and NF90. It was observed from Fig. 3(a) and 3(b) that the morphology of Nano-Pro-3012 membrane is smooth and dense with few visible pores, while the morphology of NF90 membrane has structure showing interwinning fibrous network with numerous pores. ImageJ was used to threshold the images in order to visualize the pores, and the results confirmed that the fluxes in Fig. 2 were influenced by the pore size of the membranes.

3. Rejection Behavior of Salts

The rejection of metal ions and solute flux were plotted against the filtration time for the different concentration of ions in the solution at constant pressure 10 bar, constant pH 2 and constant temperature 25 °C as shown in Fig. 4. Usually for nanofiltration membranes, flux decreases with time because of the increase in osmotic pressure by increasing concentration at the membrane surface but permeate quality remains the same [31]. It was observed in Figs. 4(a) and 4(b) that the rejection of metals is reduced with increase in operating time for the different metals, with magnesium and nickel having highest rejection for the two nanofiltration membranes. Fe^{2+} behaved differently from other ions; the rejection of Fe^{2+} decreases because the concentration of Fe^{2+} in the feed increases. An explanation to

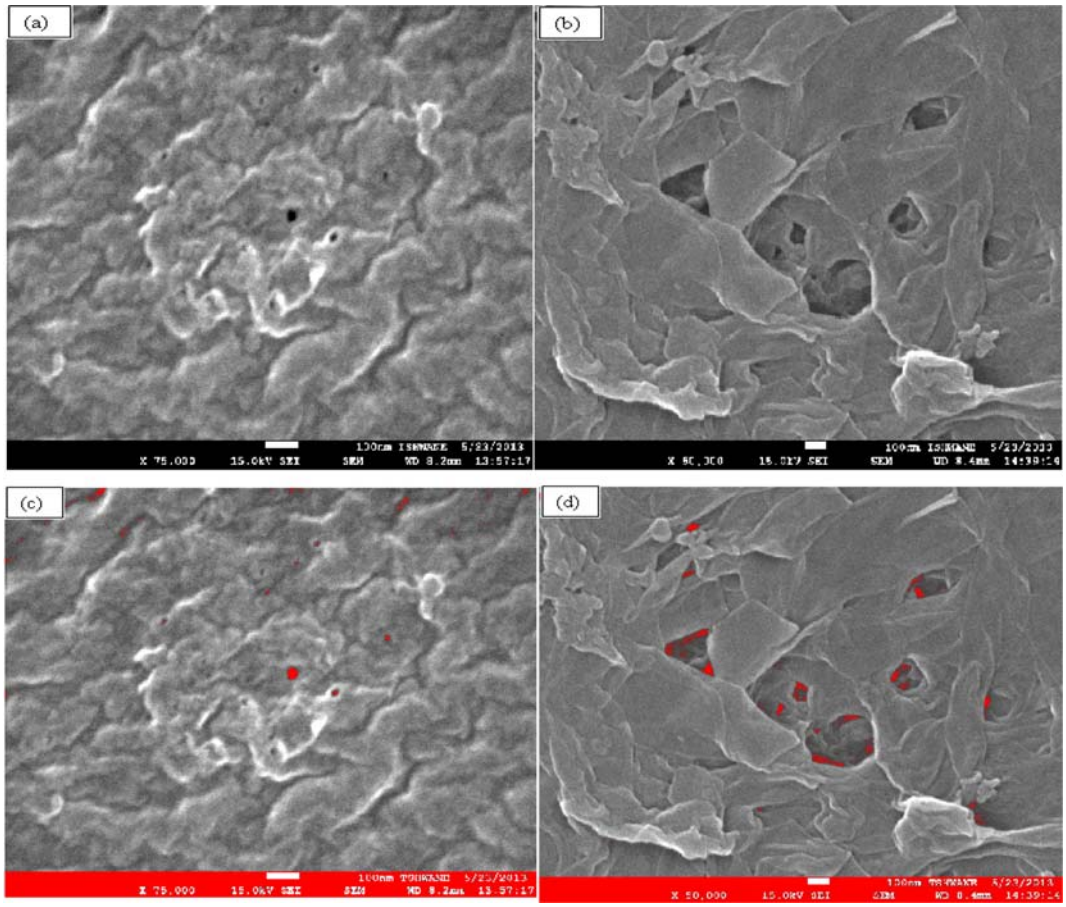

Fig. 3. (a) Original image of Nano-Pro-3012, (b) Original image of NF90, (c) Threshhold image of Nano-Pro-3012 and (d) Threshhold image of NF90. The structure of Nano-Pro-3012 membrane was dense and compact with few visible pores. NF90 membrane structure shows an intertwining fibrous network with numerous pores.

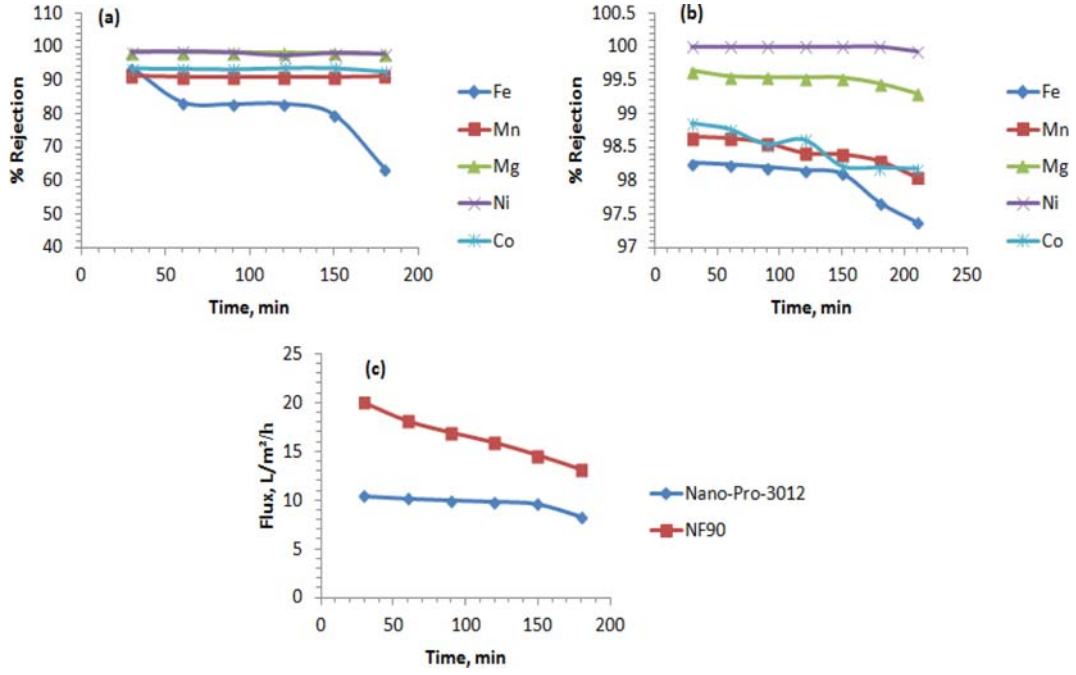

Fig. 4. (a) %Rejection as a function of time for Nano-Pro-3012, (b) %Rejection as a function of time for NF90 and (c) Fluxes of solute as function of time. The rejection sequence of these cations can be found by comparing the diffusion coefficients of the different cations. Flux decreases with time due to increase in osmotic pressure as a result of increase in concentration at the membrane surface.

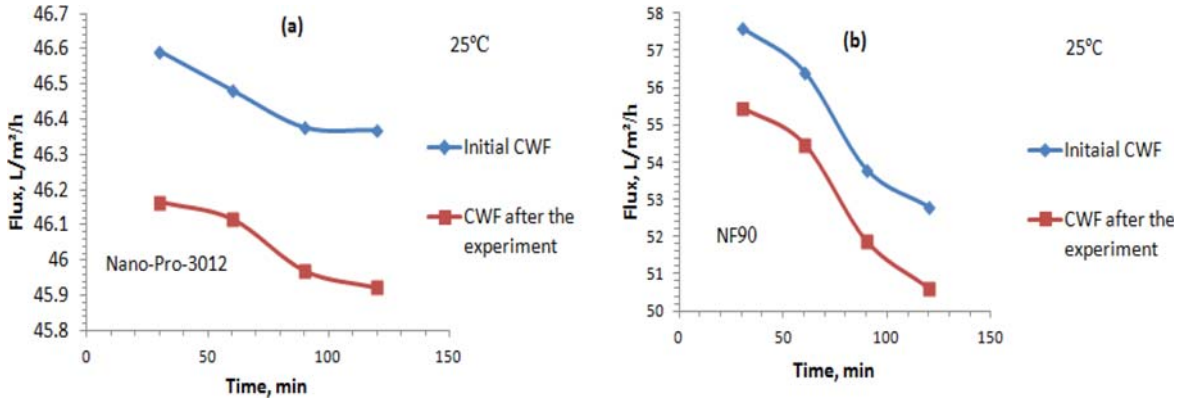

Fig. 5. Fluxes of deionized water as function of time; (a) Nano-Pro-3012 (b) NF90; The rate of flux reduction of the clean water flux experiment of NF90 was higher than Nano-Pro-3012; the percentage flux reduction for NF90 was 3.6% while the percentage water reduction for Nano-Pro-3012 was 0.98%.

this behavior is that when concentration of feed increases, both the convection and diffusion of the uncharged solute species increase, resulting in additional decrease of its rejection.

An explanation for comparing the rejection sequence of these cations can be found by comparing the diffusion coefficients of the different cations [32]. The diffusion coefficients of Co^{2+}, Fe^{2+}, Mn^{2+}, Mg^{2+} and Ni^{2+} in water at 25 °C are 1.46×10^{-5} cm^2/s 1.438×10^{-5} cm^2/s, 1.424×10^{-5} cm^2/s, 1.412×10^{-5} cm^2/s and 1.32×10^{-5} cm^2/s, respectively [33]. It was assumed that the diffusion coefficients in a membrane can be approximated by those in aqueous solutions. The order of diffusion coefficients is inversely reflected in the rejection sequence, so that diffusion seems to be an important transport mechanism [32]. As the diffusion coefficients of Co^{2+}, Fe^{2+}, Mn^{2+} are slightly higher than those of Ni^{2+} and Mg^{2+}, a high diffusion contribution may be expected, resulting in a lower rejection of Co^{2+}, Fe^{2+}, Mn^{2+}; similar trends were observed in the literature [32,34]. The minor loss in the rejection of some of these metal ions may also be due to the minor decrease in solvent permeability as a result of the reduction in flux (Fig. 4(c)). It is observed in Fig. 4(c) that the flux decreases with time due to increase in osmotic pressure as a result of increase in concentration at the membrane surface.

4. Clean Water Fluxes Before and After Exposure of the Membranes to the Mixed Salts Solution

The deposition of colloidal particles on membranes during filtration processes results in the formation of a cake layer, which decreases the permeate flux. The clean water fluxes of the initial and final (after exposure of the membrane) are shown in Fig. 5. The initial clean water fluxes of the two nanofiltration membranes were higher than the clean water fluxes after exposure of the membranes to the solution. This indicated that the membrane surface was affected by the solution. Therefore, care should be taken to pretreat the water properly prior to treatment of wastewater to prevent fouling of the membrane. Also, the rate of flux reduction of the clean water flux experiment of NF90 was higher than Nano-Pro-3012; the percentage flux reduction for NF90 was 3.6%, while the percentage water reduction for Nano-Pro-3012 was 0.98%. The percentage flux reduction was calculated using Eq. (3b).

5. Surface Roughness Analysis of Nano-Pro-3012 and NF90 with Atomic Force Microscopy

The surface roughness is an important structural property of nanofiltration membranes [24]. It has been shown that it can be related to colloidal fouling [7,8]. Figs. 6(a) and 6(c) show the noncontact mode images obtained from AFM for 1.0 μm×1.0 μm and 5.0 μm×5.0 μm neat NF90 and Figs. 6(b) and 6(d) show the corresponding 3D topography images of the same membrane areas. The topography images represent the membrane top views with the information on the depth of the membranes in the Z-direction coded in color intensity with the light regions having the highest points represent the peaks and the dark region represents the pores. The images show a topography feature with fine network like fibrous structure and the three-dimensional orthographic images show the occurrence of the peaks and the valleys. An average roughness of a membrane is defined as an average deviation of peaks and valleys from the mean plane, i.e., the average of all height obtained by atomic force microscopy analysis [7]. Figs. 7(a) and 7(c) show the noncontact mode images obtained from atomic force microscopy for 1.0 μm×1.0 μm and 5.0 μm×5.0 μm neat Nano-Pro-3012, and Figs. 7(b) and 7(d) show the corresponding three-dimensional topography images of the same membrane areas. The images different topography feature with NF90; Nano-Pro-3012 have a thick structure and higher ridges of three-dimensional orthographic. These ridges could be due to manufacturing artefacts and could be useful landmarks when investigating the fouled Nano-Pro-3012. If the original patterns (ridges) are seen in the fouled cases, then it can be summarized that there was very little deposition on the membrane surface.

6. Surface Roughness Analysis of Nano-Pro-3012 and NF90 with Scanning Electron Microscopy (SEM)

The scanning electron micrograph of neat NF90 and Nano-Pro-3012 membranes at two magnifications are shown in Fig. 8. The bar scale in NF90 and Nano-Pro-3012 membranes of lower magnification (Figs. 8(a) and 8(c)) are 1 μm. The membranes appear relatively smooth at this scale with Nano-Pro-3012 membrane smoother and denser than NF90 because the pores are not visible. The bar scale in NF90 and Nano-Pro-3012 membranes of lower magnification (Figs. 8(b) and 8(d)) are 100 nm. The roughness of NF90 membrane (Fig. 8(b)) is more apparent at this scale and the structure shows interwinning fibrous network with numerous pores, while the roughness of Nano-Pro-3012 membrane (Fig. 8(d)) shows that the membrane is very dense and not very porous. One would expect Nano-Pro-3012 membrane to have relatively high fouling on its

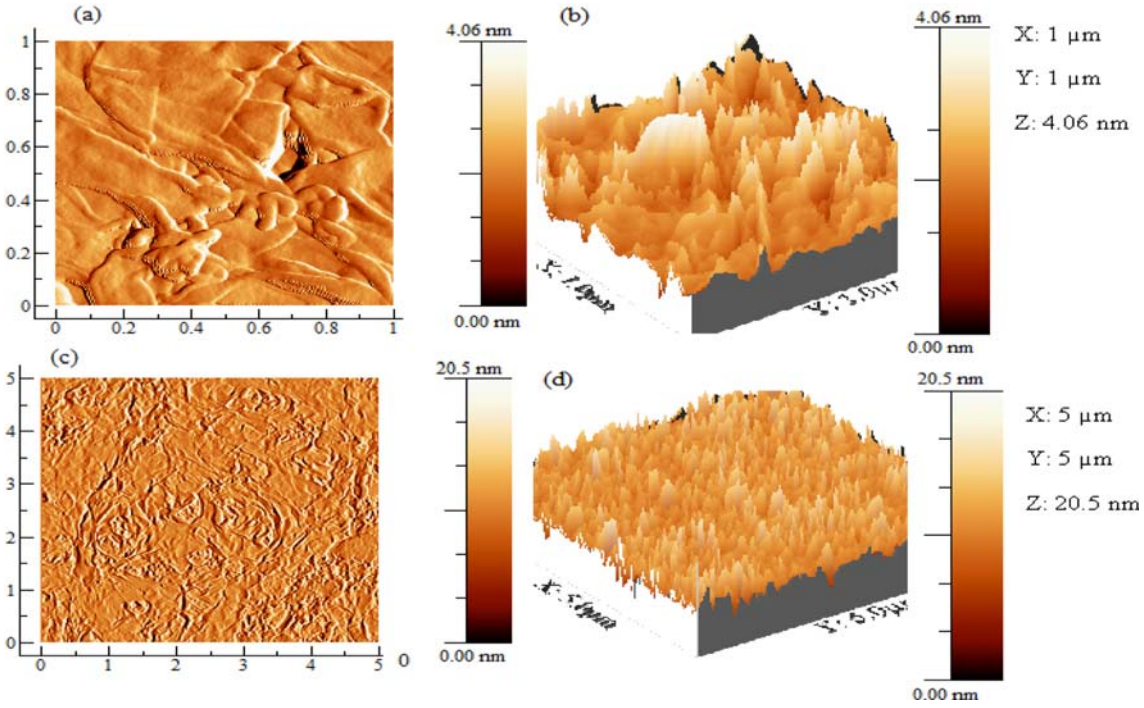

Fig. 6. (a) AFM topography image of 1.0 μm×1.0 μm neat NF90, (b) 3D orthographic image with the vertical scale enhanced to amplify the surface morphology of 1.0 μm×1.0 μm neat NF90 (4.06 nm/division for the Z scale compared to 1 μm/division for X and Y scale, (c) AFM topography image of 5.0 μm×5.0 μm neat NF90, (d) 3D orthographic image with the vertical scale enhanced to amplify the surface morphology of 5.0 μm×5.0 μm neat NF90 (20.5 nm/division for the Z scale compared to 5 μm/division for and Y scale.

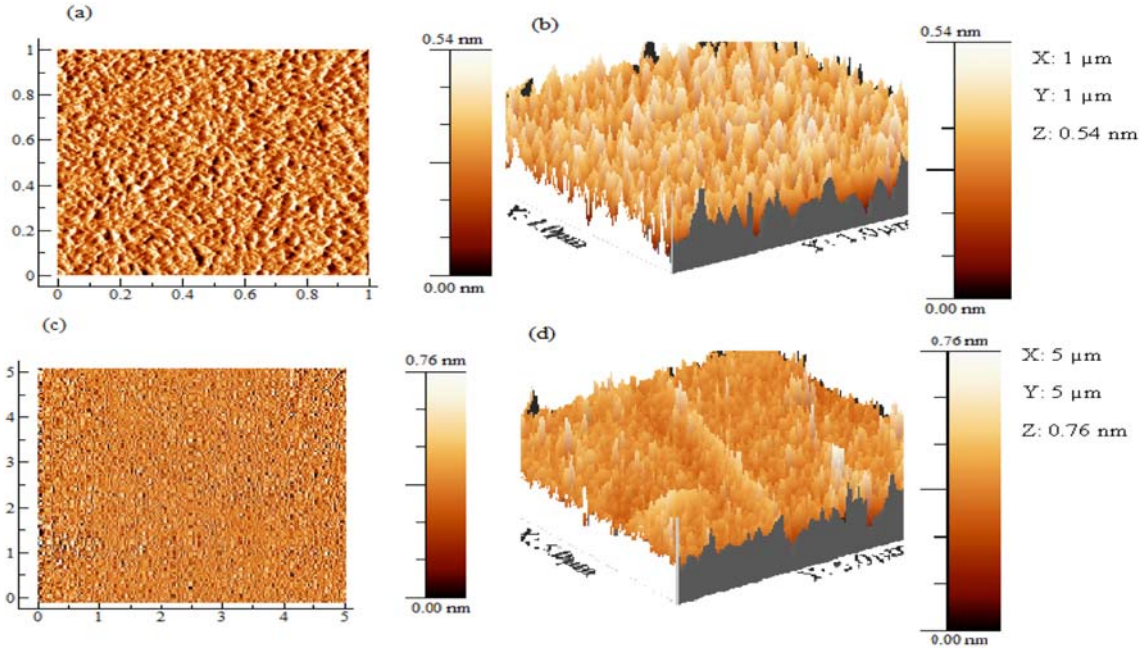

Fig. 7. (a) AFM topography image of 1.0 μm×1.0 μm neat Nano-Pro-3012, (b) 3D orthographic image with the vertical scale enhanced to amplify the surface morphology of 1.0 μm×1.0 μm neat Nano-Pro-3012 (0.54 nm for the Z scale compared to 1 μm/ division for X and Y scale, (c) AFM topography image of 5.0 μm 5.0 μm neat Nano-Pro-3012, (d) 3D orthographic image with the vertical scale enhanced to amplify the surface morphology of 5.0 μm×5.0 μm neat Nano-Pro-3012 (0.76 nm/division for the Z scale compared to 5 μm/division for X and Y scale.

surface because of the dense nature, but, on the contrary, the fouling on the surface was not much. Nano-Pro-3012 has 0.98% flux reduction after the exposure of the membrane to the solution, while NF90 has 3.6% flux reduction after the exposure of the membrane to the

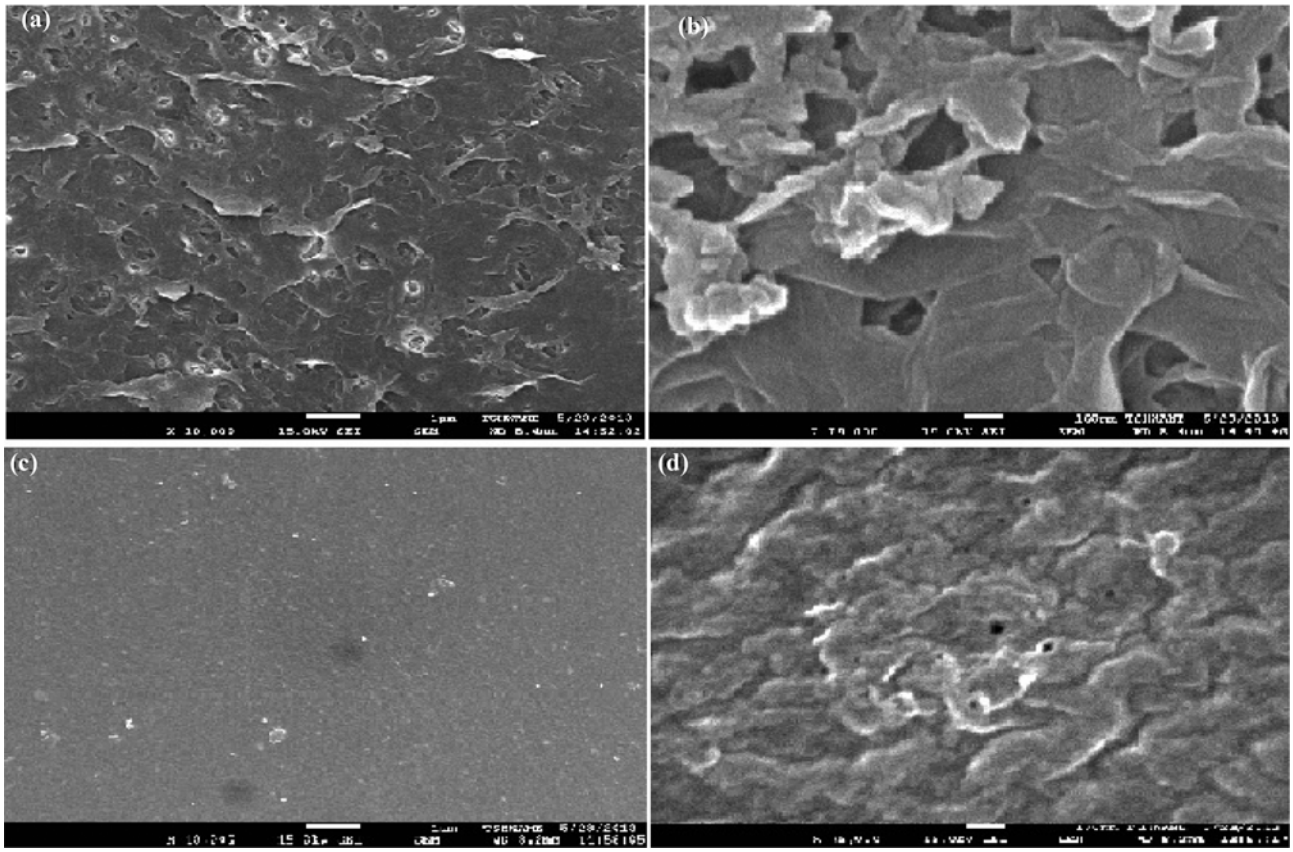

Fig. 8. (a) SEM micrograph of NF90 at lower magnification, (b) SEM micrograph of NF90 at higher magnification, (c) SEM micrograph of Nano-Pro-3012 at lower magnification and (d) SEM micrograph of Nano-Pro-3012 at higher magnification.

solution (see Fig. 5).

The height information of these membranes is however not recorded in the 2D images of SEM; it is therefore difficult to find the height variation (roughness) of these images. We therefore decided to analyze the SEM images with ImageJ software to determine the height roughness from these images. The 3D images of SEM follow the same trend with the 3D AFM for both NF90 and Nano-Pro-3012. The topography feature of NF90 has fine network-like fibrous structure with the occurrence of the peaks and the valleys. Nano-pro-3012 has a thick structure and higher ridges of 3D orthographic with the lower magnification denser than the higher magnification.

7. Neat Membrane Bearing Analysis

Due to the effect of image size on various roughness parameters, surface roughnesses were compared for identical scan sizes for 1.0 μm×1.0 μm scan areas. Fig. 10 shows the bearing analysis plot of the neat membranes (NF90 and Nano-Pro-3012). The height distribution of 4.06 nm of NF90 was of small width in comparison to the length: centered at the peak value of 2 nm while the height distribution of Nano-Pro-3012 was lower, centered at the peak value of 0.25 nm), broader and less symmetrical. There was less regularity in the surface structure of Nano-Pro-3012. The surface of Nano-Pro-3012 membrane was fairly smooth compared to NF90 membrane; however, the rougher was less compared to NF90 with peaks 0.25 nm in height. As discussed in section 3.5.1, Nano-Pro-3012 membrane exhibits the characteristic ridge pattern which was evident in the two-dimensional plot. Given the AFM topography image (Figs. 7) and SEM micrograph (Figs. 8(c) and 8(d)) of this membrane, a less rough surface was anticipated. The surface roughness of nano-filtration membranes can be attributed to a factor proportional to the bond strength of the membranes. The higher roughness parameters of the neat NF90 leads to greater adhesive strength of the NF90 and greater efficiency in the separation process [35]. Summary of the parameters that were used to quantitatively describe the surface roughness of the neat membranes is given in Tables 3 and 4. Comparing the statistical roughness data obtained for the atomic force microscopy and scanning electron microscopy using WXSM 5.0 and ImageJ software, respectively, it can be concluded that the morphology statistics for the two softwares are quite similar, but NF90 membrane appears to be rougher compared to Nano-Pro-3012. The atomic force microscopy and scanning electron microscopy analysis done with WXSM 5.0 and ImageJ software, respectively, gave a negative skewness for NF90 and positive skewness for Nano-Pro-3012. The negative skew values correspond to dominance of valley associated with a porous-like surface (i.e., NF90 has a porous surface), while the positive skew values of Nano-Pro-3012 (Tables 3 and 4) peaks dominate the surface of the membrane. The atomic force microscopy and scanning electron microscopy using analysis done with WXSM 5.0 and ImageJ software, respectively, gave a positive kurtosis for NF90 and Nano-Pro-3012. The kurtosis of NF90 was above 3; this suggests a sharp height distribution, while the kurtosis of Nano-Pro-3012 which was below 3 (Tables 3 and 4) suggests Gaussian distribution, indicating a flat and repetitive surface.

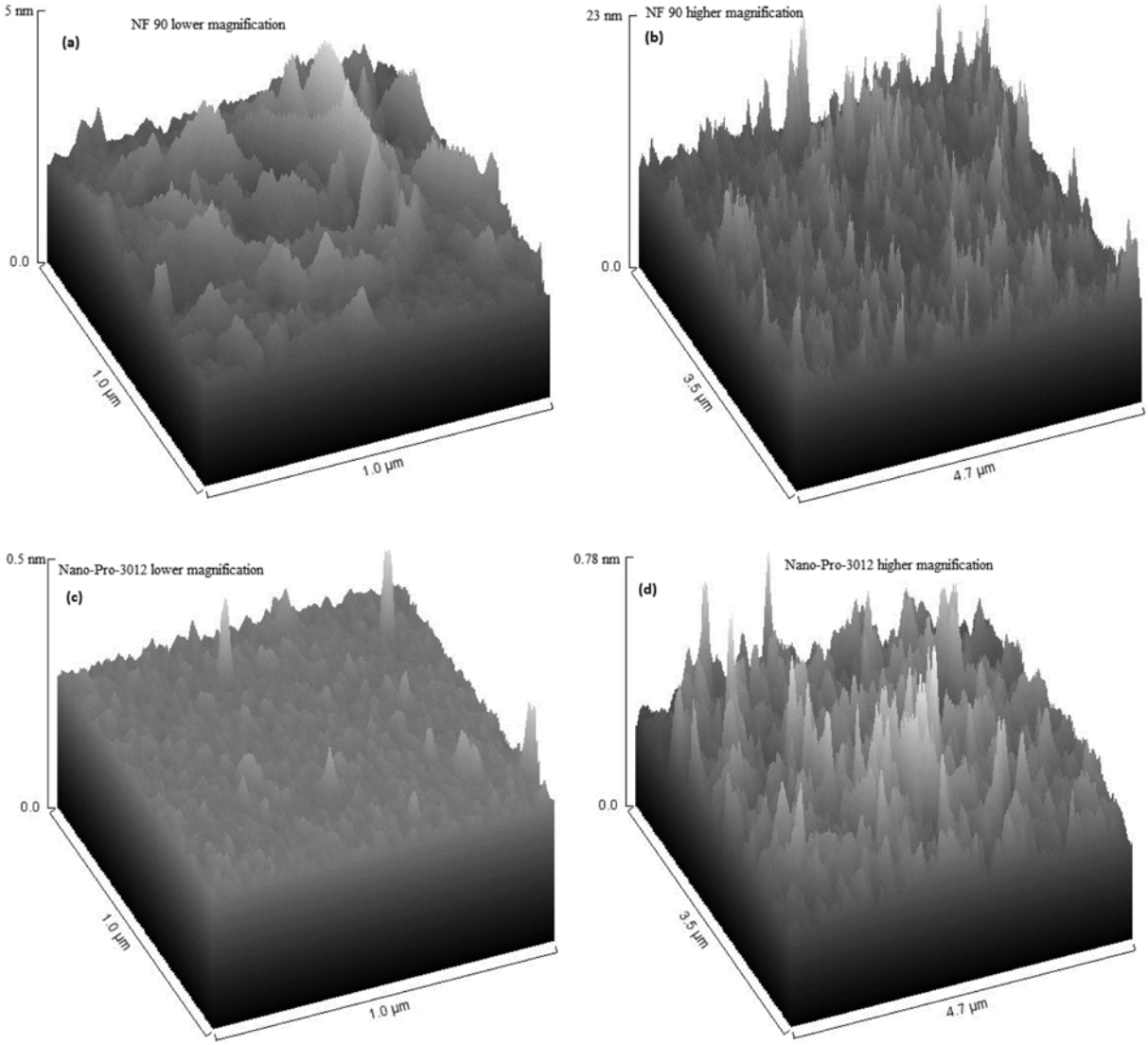

Fig. 9. (a) 3D SEM of NF90 at lower magnification, (b) 3D SEM of NF90 at higher magnification, (c) 3D SEM of Nano-Pro-3012 at lower magnification and (d) 3D SEM of Nano-Pro-3012 at higher magnification. NF90 has fine network like fibrous structure with the occurrence of the peaks and the valleys, while Nano-Pro-3012 has thick texture and higher ridges of 3D orthographic with the lower magnification denser than the higher magnification.

Table 3. AFM summary of the statistical parameters that were used to quantitatively describe the surface roughness of the neat membranes (1.0 μm×1.0 μm scan areas) with the aid of WXSM 5.0 software

Morphological parameters	Units	NF90	Nano-Pro-3012
rms roughness	nm	260±20	16±5
Peak to peak value	-	4.1	0.51
Mean roughness	nm	67	19
Average height	nm	4.06	0.54
Surface skewness	-	−0.0033	0.289
Surface kurtosis	-	6.6	2.59

Table 4. Scanning electron microscopy summary of the statistical parameters that were used to quantitatively describe the surface roughness of the neat membranes (lower magnification) with the aid of ImageJ software

Morphological parameters	Units	NF90	Nano-Pro-3012
Mean roughness	nm	263±10	17±5
Average height	nm	5	0.5
Surface skewness	-	−0.38	0.09
Surface kurtosis	-	8.73	1.23

8. Bearing Analysis of Fouled Membranes

The bearing analysis of metal ions after filtration experiment provides quantitative information of what fraction of the deposited particles are located at a specific reference plane. Fig. 11 shows the result of a bearing analysis performed for a reference plane height of 44.27 nm and 46.6 nm for NF90 and Nano-Pro-3012, respectively. The height distributions were centered on a peak for each membrane. The high peak in NF90 was at 7.09 nm and the high peak in Nano-Pro-3012 was at 6.8 nm. Both distributions have long tails above their peaks as a result of wide distribution of smaller peaks. These

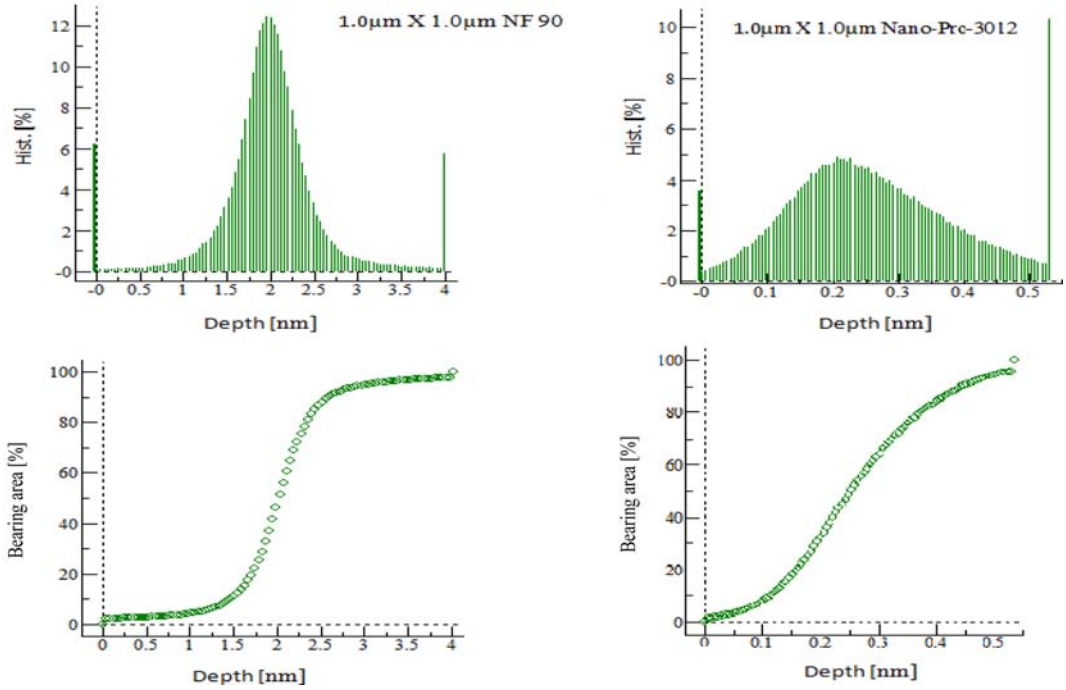

Fig. 10. 1.0 μm×1.0 μm Bearing analysis of atomic force microscopy height image of neat membranes (left; NF90) and (right Nano-pro-3012) displaying the depth distribution and the bearing analysis.

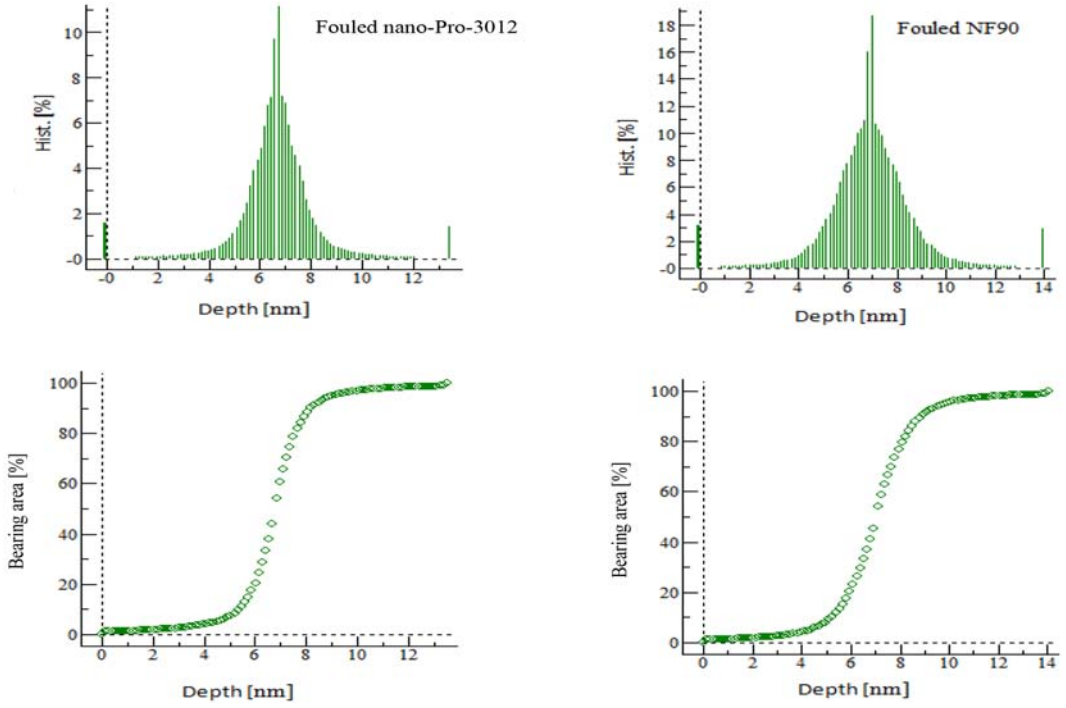

Fig. 11. Bearing analysis of fouled membranes (left: Nano-Pro-3012; right NF90). The height distributions were centered on a peak for each membrane. The high peak in NF90 was at 7.09 nm and the high peak in Nano-Pro-3012 was at 6.8 nm.

peaks are evident in the two-dimensional images accompanying the bearing analyses. The depth distribution of the membranes in Fig. 11 aids in the estimation of surface coverage. The particle deposition rate on the surface of the membranes was due to the permeation drag, which is the predominant cause of particle deposition onto the surface of the membranes. Going by the depth distribution of NF90, the particle deposition rate was higher than Nano-Pro-3012. Since the original patterns (ridges) seen in the neat Nano-Pro-3012 are not seen in the fouled Nano-Pro-3012, then it can be summarized that there was some deposition on the membrane surface; this was evident in Figs. 5 and 11. The two-dimensional images of the fouled membranes are shown in Fig. 12; here, the particles

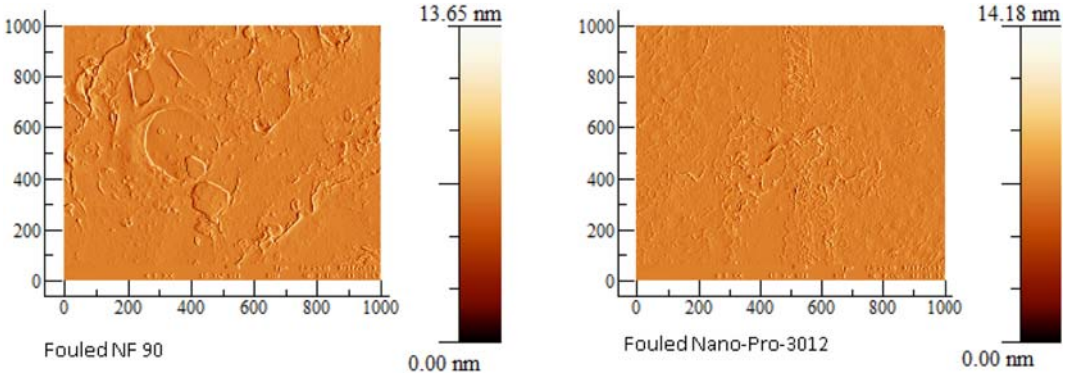

Fig. 12. Two-dimensional images of fouled membranes show that the membranes are affected by the metal.

of metal deposit on the membranes after three hours of filtration show that NF90 is more prone to fouling than Nano-Pro-3012. It was also observed from Fig. 11 that the membrane material strongly affects the way in which a surface is fouled, i.e., the pore structure and the roughness. The performance of the membranes was also very different because they have different surface characteristics; this was observed from the permeate reduction in Fig. 5. The reduction of flux with time shows that there was an increase in the metals deposited on the surface of the membranes.

CONCLUSION

Fouling is the drop in permeate flux due to the accumulation of materials in the pores and on the surface of a membrane. The fouling of rough nanofiltration membranes by toxic metal particles was studied with a dead end cell. The deposition of particles on a membrane during membrane filtration leads to formation of a cake layer, which decreases the permeate flux. The nanoscale surface characterization of the membranes using atomic force microscopy and scanning electron microscopy revealed a regulated evolution in nanomorphology and physical properties of the membranes. Atomic force microscopy and scanning electron microscopy imagery of the clean membranes give very useful qualitative impressions of differences between the membranes used in this experiment. The bearing analysis of the images indicated the depth distribution of deposit on the surface coverage around the peaks and ridges of the membranes. NF90 membrane was found to be more prone to fouling than the Nano-Pro-3012 membrane. The main factor in permeate flux reduction due to fouling was the particles of the toxic metals that are physically or chemically retained in the pores.

ACKNOWLEDGEMENTS

The research described in the paper was financially supported by THRIP and NRF.

REFERENCES

1. J. C. Mierzwa, C. D. Vecitis, J. Carvalho, V. Arieta and M. Verlage, *J. Membr. Sci.*, **421**, 91 (2012).
2. R. J. Petersen, *J. Membr. Sci.*, **83**, 81 (1993).
3. M. Dalwani, N. E. Benes, G. Bargeman, D. Stamatialis and M. Wessling, *J. Membr. Sci.*, **363**, 118 (2010).
4. K. Boussu, B. van der Bruggen, A. Volodin, C. van Haesendonck, J. A. Delcour, P. van der Meerenf and C. Vandecasteele, *Desalination*, **191**, 245 (2006).
5. M. Hirose, H. Ito and Y. Kamiyama, *J. Membr. Sci.*, **121**, 209 (1996).
6. M. Elimelech, X. Zhu, A. E. Childress and S. Hong, *J. Membr. Sci.*, **127**, 101 (1997).
7. E. M. Vrijenhoek, S. Hong and M. Elimelech, *J. Membr. Sci.*, **188**, 115 (2001).
8. E. M. V. Hoek, S. Bhattacharjee and M. Elimelech, *Langmuir*, **19**, 4836 (2003).
9. A. C. Sagle, E. M. Van Wagner, H. Ju, B. D. McCloskey, B. D. Freeman and M. M. Sharma, *J. Membr. Sci.*, **340**, 92 (2009).
10. M. Bauman, A. Košac, A. Lobnik, I. Petrini and T. Luxbacher, *Colloids Surf. A.*, **422**, 110 (2013).
11. I. M. El-Nahhal and N. M. El-Ashgar, *J. Organomet. Chem.*, **692**, 2861 (2007).
12. E. M. Van Wagner, A. C. Sagle, M. M. Sharma, Y. H. La and B. D. Freeman, *J. Membr. Sci.*, **367**, 273 (2011).
13. V. Freger, A. Bottino, G. Capannelli, M. Perry, V. Gitis and S. Belfer, *J. Membr. Sci.*, **256**, 134 (2005).
14. F. A. Pacheco, I. Pinnau, M. Reinhard and J. O. Leckie, *J. Membr. Sci.*, **358**, 51 (2010).
15. N. Hilal H. Al-Zoubi, N. A. Darwish and A. W. Mohammad, *Desalination*, **117**, 187 (2005).
16. H. Ivnitsky, I. Katz, D. Minz, G. Volvovic, E. Shimoni, E. Kesselman, R. Semiat and C. G. Dosoretz, *Water Res.*, **41**, 3924 (2007).
17. M. J. Skaug, R. Faller and M. L. Longo, *J. Chem. Phys.*, **134**, 1 (2011).
18. A. W. Mohammad, N. Hilal, L. Y. Pei, I. N. H. M. Amin and R. Raslan, *Saina Malaysiana*, **40**, 237 (2011).
19. R. Tamime, Y. Wyart, L. Siozade, I. Baudin, C. Deumie, K Glucina and P. Moulin, *Membranes*, **1**, 91 (2011).
20. M. Pontié, A. Thekkedath, K. Kecili, H. Dach, F. De Nardi and J. B. Castaing, *Desalination*, **292**, 73 (2012).
21. J. E. Sader, J. A. Sanelli, B. D. Adamson, J. P. Monty, X. Wei, S. A. Crawford, J. R. Friend, I. Marusic, P. Mulvaney and J. Bieskes, *Rev. Sci. Instrum.*, **83**, 1 (2012).
22. K. C. Khulbe and T. Matsuura, *Polymer*, **41**, 1917 (2000).
23. K. Boussu, B. Van der Bruggen, A. Volodin, J. Snauwaert, C. Van Haesendonck and C. Vandecasteele, *J. Colloid Interface Sci.*, **286**, 632 (2005).

24. J. Stawikowska and A. G. Livingston, *J. Membr. Sci.*, **425**, 58 (2013).
25. L. Song, P. R. Johnson and M. Elimelech, *Environ. Sci. Technol.*, **28**, 1164 (1994).
26. L. Song and M. Elimelech, *J. Colloid Interface Sci.*, **167**, 301 (1994).
27. J. A. Brant, K. M. Johnson and A. E. Childress, *Colloids Surf. A.*, **280**, 45 (2006).
28. K. Boussu, A. Belpaire, A. Volodin, C. van Haesendonck, P. Van der Meeren, C. Vandecasteele and B. van der Bruggen, *J. Membr. Sci.*, **289**, 220 (2007).
29. A. I. Schäfer, N. Andritosos, A. J. Karabelas, E. M. V. Hoek, R. Schneider and M. Nyström., *Fouling in nanofiltration, nanofiltration-principles and applications*, Elsevier Advanced Technology, UK (2004).
30. I. Horcas, R. Fernandez, J. M. Gomez-Rodriguez, J. Colchero, J. Gomez-Herrero and A. M. Baro, *Rev. Sci. Instrum*., **78**, 1 (2007).
31. J. S. Taylor, D. M. Thompson and J. K. Carswell, *J. AWWA*, **79**, 72 (1987).
32. L. B. Chaudhari and Z. V. P. Murthy, *J. Environ. Res. Dev.*, **3**, 400 (2008).
33. P. Vanysek, *Ionic conductivity and diffusion at infinite dilution in: CRC Handbook of Chemistry and Physics*, 90th Ed., CRC Press, Boca Raton, Florida, 5 (2005).
34. A. W. Mohammad, R. Othaman and N. Hilal, *Desalination*, **168**, 241 (2008).
35. W. R. Bowen, N. Hilal, R. W. Lovitt and C. J. Wright. *J. Membr. Sci.*, **139**, 269 (1998).